MATERIALS SCIENCE

Organic monolayers disrupt plastic flow in metals

Tatsuya Sugihara[1]*, Anirudh Udupa[2]*, Koushik Viswanathan[3], Jason M. Davis[2,4], Srinivasan Chandrasekar[2†]

Adsorbed films often influence mechanical behavior of surfaces, leading to well-known mechanochemical phenomena such as liquid metal embrittlement and environment-assisted cracking. Here, we demonstrate a mechanochemical phenomenon wherein adsorbed long-chain organic monolayers disrupt large-strain plastic deformation in metals. Using high-speed in situ imaging and post facto analysis, we show that the monolayers induce a ductile-to-brittle transition. Sinuous flow, characteristic of ductile metals, gives way to quasi-periodic fracture, typical of brittle materials, with 85% reduction in deformation forces. By independently varying surface energy and molecule chain length via molecular self-assembly, we argue that this "embrittlement" is driven by adsorbate-induced surface stress, as against surface energy reduction. Our observations, backed by modeling and molecular simulations, could provide a basis for explaining diverse mechanochemical phenomena in solids. The results also have implications for manufacturing processes such as machining and comminution, and wear.

INTRODUCTION

Changes in surface dynamics in the presence of a chemical film have been the subject of curiosity since at least Mesopotamian times (*1*, *2*). Seafarers in Europe, dating back to Pliny the Elder (*3*), would often empty oil barrels into the sea—forming a thin monomolecular oil layer over the water surface—to "still the waves." This seemingly dubious phenomenon, first systematically investigated by Ben Franklin (*4*), involves a coupling between interface energetics and free-surface kinematics (*5*)—a so-called mechanochemical (MC) effect. In solids, similar coupling can lead to a wider variety of MC phenomena, all characterized by either anomalous deformation or crack growth or wear under external loading. Several apparently disparate examples are noteworthy: environment-assisted cracking, where certain chemical environments can promote catastrophic brittle fracture of otherwise ductile substrates (*6*–*10*), the Bangham effect, involving swelling and deformation of nanoporous solids by physisorption of suitable fluids (*11*, *12*), and the more widely reported Rehbinder effect and its variants, entailing apparent surface energy reduction and associated change in material deformation with certain metal-film combinations (*13*–*17*).

Despite several reports of these effects, fundamental questions about the underlying mechanisms remain unanswered. Take the case of embrittlement effects in metals, for which the most common explanation is that an adsorbed surface film reduces the fracture stress by lowering surface energy (*18*). One class of embrittling phenomena in metals might be driven by this cohesive energy reduction via solute segregation at grain boundaries (*19*, *20*). However, this cannot be the mechanism for most MC phenomena, as the diffusivity of the adsorbate molecules into the solid is often negligible (*8*, *21*).

Driven by recent observations of adsorbate-induced anomalous force reduction in plastic deformation of metals (*22*–*24*), we present a unique MC effect mediated by organic self-assembled monolayer (SAM) films. This effect is prominently manifest as a dramatic disruption of plastic flow at the metal surface, despite little change in the metal's bulk properties. The result is observed on the mesoscale as a fundamental transition in the mode of plastic flow, from unsteady sinuous (*22*, *25*), that is characteristic of ductile metals, to a quasi-periodic segmented mode, that is typical of brittle systems. By independently varying the surface energy and molecule chain length of the SAM films, we argue that this apparent embrittlement is driven by adsorption-induced surface stress, as opposed to surface energy reduction. Our observations, coupled with an analytical model, could form the basis for also explaining varied MC effects in solids such as environment-assisted cracking.

RESULTS

Experimental results

We used annealed commercially pure aluminum (Al 1100) as our base metal sample (henceforth workpiece) on which to deposit SAM films. A SAM molecule consists of a head group that bonds strongly (chemisorbed) with the substrate, a hydrocarbon chain, and a terminal group (Fig. 1A) (*26*). The use of SAM molecules allows us to alter the surface energy γ and surface stress f independently. While the terminal and head groups determine the free surface and monolayer-metal interface energies, respectively, the surface stress can be varied by changing the hydrocarbon chain length (*27*, *28*), analogous to the Traube rule in liquids (*29*). Aluminum was chosen for three reasons—its thin stable oxide film allows easy deposition of different SAM molecules; it shows very high ductility in the annealed state, making film effects on plastic flow readily observable; and its deformation characteristics are typical of technologically relevant systems like stainless steels and Ni alloys.

To create the molecular film, the workpiece surface was plasma-treated and immersed in a 1 mM solution of the SAM molecule in ethanol and rinsed in water (Fig. 1B) (see Materials and Methods) (*30*, *31*). Five of the six SAM molecules used had the same silane-based head and CH_3 terminal groups, but with carbon chain lengths between 3 and 16, denoted by $CH_3(3)$, $CH_3(6)$, $CH_3(8)$, $CH_3(10)$, and $CH_3(16)$, with the number in the bracket indicating

[1]Department of Mechanical Engineering, Osaka University, Suita, Osaka 565-0871, Japan. [2]Center for Materials Processing and Tribology, Purdue University, West Lafayette, IN 47907-2023, USA. [3]Department of Mechanical Engineering, Indian Institute of Science, Bangalore 560012, India. [4]Special Warfare and Expeditionary Systems Department, Naval Surface Warfare Center, Crane Division, Crane, IN 47552, USA.
*These authors contributed equally to this work.
†Corresponding author. Email: chandy@purdue.edu

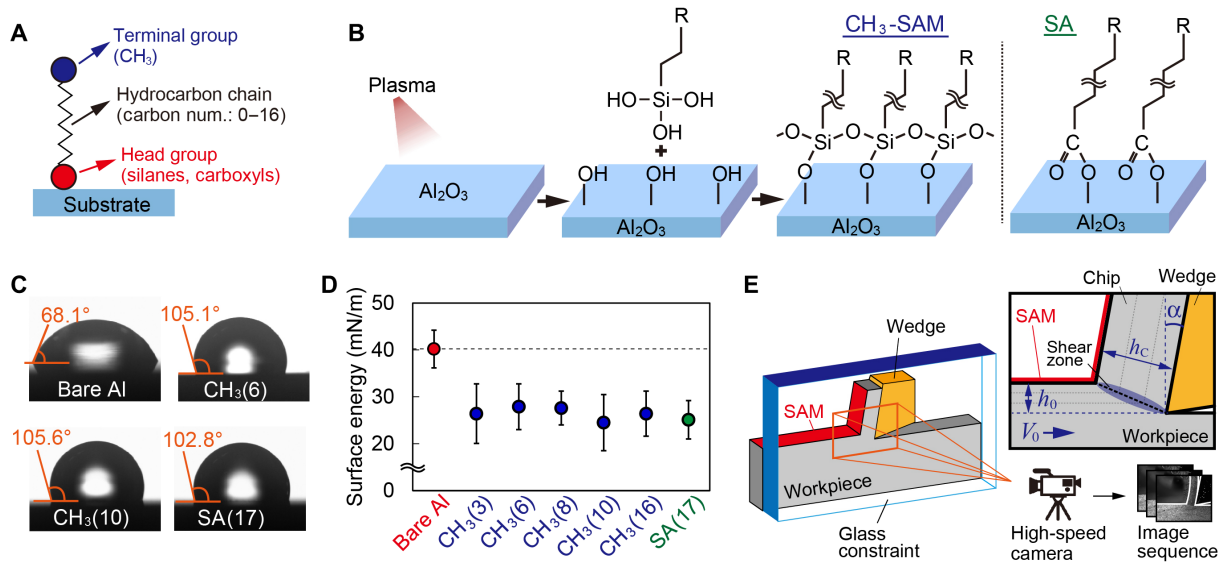

Fig. 1. Using SAMs to probe MC effect. (**A**) Schematic of a molecule adsorbed on metal surface showing head and terminal groups, and hydrocarbon chain. (**B**) Procedure to deposit SAMs: For the silane head molecules, workpiece is first plasma-treated to increase hydroxyl group density at surface and then immersed in ethanol solution containing the molecule. For the stearic acid SAM, workpiece is directly immersed in ethanol solution containing stearic acid. (**C**) SAM-deposited workpiece surfaces characterized by contact angle measurement. (**D**) Surface energy obtained from the contact angle using the Owens-Wendt theory (*34*). Because surface energy is determined purely by terminal group, all the SAMs show a uniform reduction of ~37% in this energy. (**E**) Model 2D experimental (simple shear) configuration used to explore MC effect with SAM films (red). A high-speed camera, coupled to an optical microscope, is used to image material flow and characterize plastic flow field.

chain length. In addition to these, we also used a sixth molecule, stearic acid [SA(17)], with a -COOH head group, a -CH_3 terminal group, and a 17 C chain, to study the possible influence of the head group on the MC effect.

The surface energy change due to the SAM layer was inferred using standard contact angle measurements with deionized water and hexadecane (see Fig. 1C). Because the contact angle is primarily determined by the terminal group of the molecules (-CH_3) (*32*, *33*), there was no significant difference between different SAM molecules. However, there was a marked difference between the coated (105.6°) and uncoated or bare surface (68.1°) (see Fig. 1D). The measured contact angle of the SAM-coated surface (105.6°) is consistent with that reported for a well-packed methyl surface (*32*, *33*), showing that each SAM was uniformly deposited on the surface of the specimens. Corresponding energy estimates (*34*) showed that the surface energy for the deposited SAM films was 37% lower than the bare Al (surface energy, 40 mN/m for Al_2O_3).

The effect of the SAM film on workpiece deformation behavior was studied using a model two-dimensional (2D) shear configuration (see Materials and Methods). A sharp wedge/tool was used to impose simple shear along a narrow zone, thereby "peeling" off a narrow strip (Fig. 1E). This shear loading is also representative of cutting and wear processes. The rectangular Al workpiece was moved (horizontally) at a constant velocity V_0 relative to the wedge inclined at an angle α (rake) with the vertical (see inset). Material of depth h_0 (undeformed chip) is then continuously sheared into a chip of thickness h_c ($>h_0$). The ratio $\lambda = h_c/h_0$, typically in the range of 2 to 20 depending on the mesoscale plastic deformation mode operational, provides a measure of the imposed shear strain. In the experiments, V_0 = 5 mm/s, h_0 = 50 μm, and α = 10° were fixed a priori; this low V_0 ensured near quasi-static deformation with negligible temperature effects.

The shearing experiments were done both with bare (uncoated) Al samples and with the SAM films deposited (Fig. 1E). Near-surface material (plastic) flow was imaged using a high-speed camera coupled to an optical microscope, and images were analyzed using digital image correlation (DIC) techniques to obtain material velocity, strain, and strain-rate fields in the deforming workpiece (*22*). Concurrently, deformation forces, viz, the cutting (power) component parallel to V_0 and thrust component perpendicular to V_0, were measured using a piezoelectric dynamometer. The topography of the cut surface in the wake of the wedge was characterized by optical profilometry to see how changes in flow dynamics influenced the peeling. At least five samples were tested under each condition to ensure reproducibility.

The long-chain SAM films (chain length, >8) were found to have a major influence on the workpiece deformation, thereby demonstrating an MC effect. This is quantified by comparing force components (Fig. 2A) for the various film-coated metals vis-á-vis bare Al (red curve). For bare Al, the cutting force gradually increases to a steady-state value of ~600 N; the corresponding thrust force was ~550 N. These steady-state values are exceptionally high, higher than in similar simple shearing of even hard steels (*35*). In addition, after about 6 s of deformation, periodic oscillations can be seen in the force trace due to large cracks and tears that formed on the cut surface in the wake of the wedge (see the Supplementary Materials). The arithmetic average surface roughness (R_a) on the cut surface was 12.4 μm, characteristic of a very rough surface.

As is evident from Fig. 2A, there was no difference in the force trace between the CH_3(6), CH_3(3), and bare Al cases, indicating that these molecules do not induce any MC effect. In complete contrast, with the CH_3(16), CH_3(10), and the SA(17) monolayers, the force was drastically reduced (see Fig. 2A). For the cutting force, this reduction was ~85% (steady value, 90 N) when compared to the

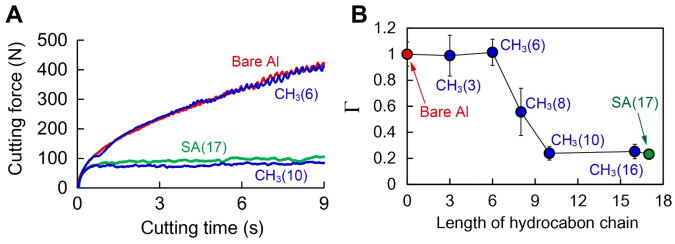

Fig. 2. Characterizing MC effect using cutting force. (**A**) Comparison of force with and without SAM films. A large force decrease (~85%), typical of the MC effect, is seen with the long-chain SAMs [CH_3(10) and SA(17)]. (**B**) Plot of the ratio (Γ)—maximum cutting force with a specific SAM film to the maximum cutting force without any film (bare)—as a function of chain length. A sharp decrease in Γ from 1 to ~0.15 occurs as chain length increases from 6 to 10, indicating the importance of chain length in controlling the MC effect.

steady-state bare Al case. A similar reduction was seen with the thrust force (steady value, 110 N). Furthermore, steady state was attained quickly (<1 s) unlike in the film-free case (>10 s), and the force traces did not show any discernible oscillations. Consequently, the cut surface was practically devoid of any tears or cracks, with R_a = 0.5 μm, an order of magnitude improvement compared to the bare Al. The force trace for CH_3(8) was intermediate between these two extremes, indicative of a partial effect.

The magnitude of the MC effect is captured by Γ, the ratio of the maximum cutting force with and without the SAM layer: $\Gamma \leq 1$, with smaller values implying stronger effect and Γ = 1 no effect. Figure 2B shows the variation in Γ with SAM molecule chain length. For bare Al, CH_3(3), and CH_3(6) molecules, Γ = 1, but sharply transitions to $\Gamma \sim 0.15$ when chain length exceeds 8. The CH_3(8) molecule gives Γ = 0.5, indicating that the MC effect is partial. The effect is strongly linked with monolayer chain length.

These force observations raise a natural question: How do the SAM films induce the MC effect in the first place? To answer this, we analyzed the development of near-surface plastic flow ahead of the wedge using in situ high-speed imaging (Fig. 3). The top row shows a set of frames from a high-speed sequence of the bare Al cutting, with the strain field and a few virtually computed streaklines overlaid. These frames were selected 1.9 s after the cutting began, and the corresponding cutting force was ~220 N. At this stage, h_c = 650 μm so that λ = 13. As the cutting progressed, h_c steadily increased to 1.3 mm, λ = 26.

It is clear in Fig. 3 (top row) that deformation in the chip is very heterogeneous—the strains vary between 3.5 and 7 and the overlaid streaklines are wavy and sinuous—indicative of severely redundant plastic flow with vortex-like components; it is for this reason that this deformation mode has been called sinuous flow (see also movie S1) (*22*, *25*). These features explain the large energy dissipation/forces characteristic of this mode (Fig. 2). To understand the mechanics of this flow, we track the motion of three initially collinear material points (green, yellow, and red; frame A1). As they approach the wedge, a bump forms on the workpiece surface, causing the yellow point to move up relative to the line connecting green and red points (frame A2). The material, then sheared and rotated, forms a large amplitude fold, thereby reducing the distance between red and green points relative to the yellow point (frame A3). The bump and subsequent fold formation repeat continuously. As a result, the folds stack up on top of each other constituting the final chip, with the interfaces between the folds resembling notches [Fig. 3, top row; see also (*22*)]. Sinuous flow was observed not only in bare Al but also with the CH_3(3)- and CH_3(6)-coated workpieces.

When the MC effect was present, i.e., reduction in cutting and thrust forces, the flow mode also fundamentally changed; see Fig. 3 (bottom row) for workpiece coated with SA(17) (see also movie S1). It is apparent that the average $h_c \sim 425$ μm, λ = 8.5, not only is now much reduced but also remains constant throughout the experiment. The chip consists of periodic segments, each with small strain (~2) zones separated by cracks appearing as narrow high-strain regions (see Fig. 3, bottom row). This deformation mode, quite distinct from sinuous flow, is referred to as segmented flow (*36*). Because the flow is dominated by periodic fracture, with relatively small-strain deformation in the segments themselves, it results in relatively low energy dissipation (forces) in the shearing experiments (Fig. 2). Besides SA(17), segmented flow was observed with all of the other long-chain molecules, that is, CH_3(10) and CH_3(16), that showed the large force reductions.

The mechanics of segmented flow may be analyzed in a manner analogous to sinuous flow, by considering the displacement of three initially collinear material points (frame B1; Fig. 3, bottom row). As the wedge advances, the yellow point moves up relative to the line connecting green and red points (frame B2). However, at this junction, a critical difference is observed. Rather than folds developing, the SA(17) film causes a crack to initiate from the workpiece-free surface and propagate toward the wedge tip between yellow and green points. The speed of the crack front is 4 mm/s, comparable to V_0. The green point continues to move toward the wedge along with the crack front and the workpiece, whereas the yellow and red points remain stationary on opposite sides of the crack, resulting in large separation (frame B3). These cracks initiate periodically from the free surface, thereby arresting the development of sinuous flow and resulting in segmented flow.

From the in situ imaging experiments and ex situ observations of chip morphology, it is clear that the role of the SAM film in the MC effect is to fundamentally alter the nature of near-surface plastic flow. More precisely, the long-chain SAM films "embrittle" the metal surface so that when the workpiece is loaded (here under simple shear), large-strain plastic deformation becomes unstable, resulting in crack propagation. Given that all the SAM molecules used had the same terminal group and reduced the surface energy by the same amount (Fig. 1D), it is reasonable to conclude that surface energy is not the cause for the MC effect. Similarly, because the head group is held constant for five of the molecules, two of which did not show an effect [CH_3(3) and CH_3(6)] and the remaining three did show the MC effect [CH_3(8), CH_3(10), and CH_3(16)], we can conclude that the head group also does not control the MC effect. Furthermore, the conventional explanation of diffusion- or segregation-induced cohesive energy change does not apply here because the diffusivity of these molecules in metals is negligible. Rather, the critical characteristic of the molecules is the length of the hydrocarbon chain—those with long chains induce the MC effect, while shorter chains do not (see Fig. 2B).

Modeling results

In light of these observations, the mechanism of the MC effect is best understood in terms of an adsorption-induced change in surface stress (*27*, *28*). Covalent adsorbate-metal interactions and van der Waals interaction of long-chain molecules seem to have a

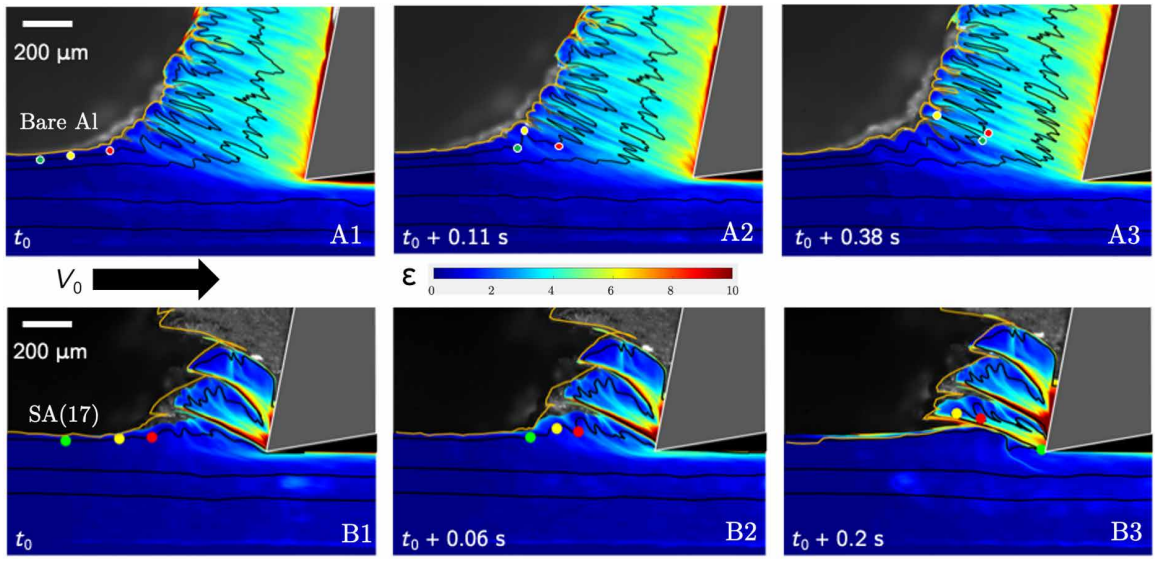

Fig. 3. High-speed imaging of (contrasting) plastic flow modes reveals origin of MC effect. Select images, with strain-field (background color) and streaklines superimposed, show development of flow with [bottom row, SA(17)] and without (top row, bare Al) long-chain SAMs. (**Top**) With bare Al workpiece, the shearing results in sinuous flow with thick-chip, wavy streaklines, and heterogeneous straining. Flow development is tracked via green, yellow, and red points (initially collinear, frame A1). A bump forms on workpiece surface ahead of chip in frame A2. The bump grows in amplitude, rotates, and shears to form a fold in frame A3. The final chip is a stack of folds, with fold interfaces resembling notches. (**Bottom**) With a long-chain SAM [SA(17)], the shearing results in segmented flow—typical of MC effect. Movement of green, yellow, and red points in frames B1 and B2 is similar to frames A1 and A2 (top row). However, between frames B2 and B3, a crack starts from workpiece surface and propagates toward wedge tip, causing a large separation between yellow and green points. This cracking, which arrests the sinuous flow in its incipient stage, is recurrent and results in segmented flow.

decisive role in determining the sign and magnitude of surface stress (*28*, *37*). Using a multiscale model of the metal-film interface (*38*), we now evaluate the response of an atomically sharp notch in the material to a remote stress. If a crack were to propagate from the notch tip at a critical stress, then the material would be brittle, while spontaneous dislocation emission from the notch tip, with associated notch blunting and lowering of stress intensity, would make the material ductile. One such notch is shown in Fig. 4A under shear loading as it enters the deformation zone ahead of the wedge. The SAM film is on the free surface (red, at arrows) extending all the way until the tip *O* and imposes a tensile surface stress of magnitude *f*. [Note that although the surface stress is a 2 × 2 tensor, it is isotropic for face-centered cubic (fcc) metals due to the threefold symmetry of the surface; thus, a single value for *f* suffices to describe the state of the surface stress (*39*).] This point *O* maybe approximated as a small vertical face with a small gap 2*d* in the film ($d \sim b \ll a$, where *b* is the Burgers vector). This heterogeneity in the film results in a force dipole of magnitude $M = 2fd$, in turn inducing a rapidly decaying ($1/\rho^2$) tensile stress at the notch tip (see the Supplementary Materials).

For this configuration (Fig. 4A), the complete stress field near *O* may be analyzed in terms of γ, *b*, *M*, the shear modulus μ, and Poisson's ratio ν of the metal using two dimensionless parameters $\zeta = \gamma(1-\nu)/\mu b$ and $\eta = M(1-\nu)/\mu b^2$, representing the contributions of surface energy and surface stress, respectively. Under the applied remote shear τ_S, two possibilities arise—if the stress intensity at *O* reaches a critical value, a crack will extend from *O*, resulting in brittle deformation (segmented flow). On the other hand, if dislocations can be spontaneously emitted from *O*, plastic deformation ensues and the notch tip will be blunted (sinuous flow). The former possibility is evaluated by balancing strain energy release and the energy required to form two new surfaces, resulting in a critical shear stress τ*. The latter is estimated by evaluating the force on a virtual edge dislocation (at *P*, perpendicular to the plane containing *OP* in Fig. 4A) located at a nondimensional distance ξ (=ρ/*b*) from *O* and along a slip plane at angle φ.

Without the SAM film, the virtual dislocation sees two opposing forces: (i) repulsion due to the external loading (Peach-Koehler force, varying as $\sqrt{\frac{1}{\xi}}$) and (ii) an attractive image force (varying as $-1/\xi$). The Peach-Koehler force dominates for $\xi \to \infty$, and the image force dominates for $\xi \to 0$; the two are balanced at an equilibrium distance $\xi = \xi^*$. With the SAM film, the additional *M*-induced $-1/\rho^2$ term makes the Peach-Koehler force attractive close to *O*, pushing ξ* further away from *O* (see the Supplementary Materials).

Balancing the two forces gives ξ* as a function of η, ζ, and ϕ

$$\sqrt{\frac{8\pi\zeta}{\xi}}\,F(\phi) - \frac{8\eta}{\xi^2}\,G(\phi) = \frac{1}{\xi} \tag{1}$$

where

$$F(\phi) = \frac{3}{2}\cos(3\phi/2) + \frac{1}{2}\cos(\phi/2) \text{ and } G(\phi) = \sin\phi\cos\phi \tag{2}$$

The solutions ξ*(ϕ) are shown in Fig. 4B as a function of ϕ (direction of dislocation slip) for μ, γ, and *b* corresponding to Al. The horizontal line ξ* = 2 (dashed) represents dislocation core radius for Al (fcc). When ξ* < 2, or the dislocation equilibrium distance is lesser than the core radius, dislocation emission is likely. When ξ* > 2, the converse happens—dislocations have to now "cross" an attractive

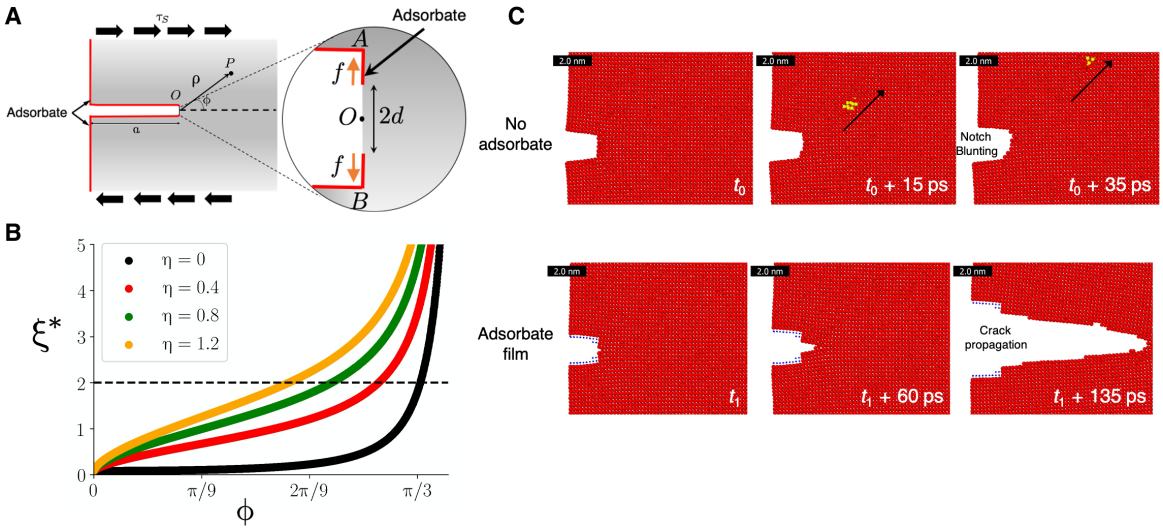

Fig. 4. Continuum and atomistic models to study adsorbate-induced embrittlement. (**A**) Schematic of adsorbate-covered notch in Al subject to remote shear loading. Notch tip is assumed locally flat with a narrow region (2*d*) free of adsorbate. The adsorbate induces a surface stress *f* on the surface, with the inhomogeneity resulting in a force dipole $M = 2fd$. A virtual dislocation is shown at point *P* (distance ρ from *O*) situated on a slip plane making angle ϕ with horizontal. (**B**) Equilibrium position of dislocation ξ* versus ϕ for various values of nondimensional surface stress η. ξ* > 2 (<2) implies brittle (ductile) behavior. As η increases, model predicts brittle behavior. (**C**) Atomistic simulations of notch behavior in ductile Al subject to remote tensile loading with and without adsorbate. Top: In the absence of adsorbate, notch emits dislocations (core marked yellow) that travel along slip plane; this emission blunts the notch (ductile). Bottom: With an adsorbate that induces surface stress $f = +3$ N/m, the atoms give way for a crack to propagate (brittle).

force barrier to reach their equilibrium position. Now, crack growth is energetically more favorable so that brittle deformation and onset of segmentation results. Consequently, ξ* = 2 represents the critical value for the transition from ductile to brittle behavior and the consequent MC effect.

The various ξ* curves shown in Fig. 4B intersect the ξ* = 2 line at different ϕ, indicating the slip plane orientations along which dislocation emission is allowed as a function of the dimensionless parameter η and for fixed ζ (Al). The model being isotropic yields a superset of all allowed dislocation slip directions; the local crystal symmetry picks out a discrete subset of these directions.

The model can help explain several seemingly contradictory experimental observations. First, ζ is unchanged by the SAM film, because it is the cohesive energy required to form two new surfaces in the bulk metal. This explains why terminal group chemistry is unimportant for the MC effect (Fig. 3), although it changes the surface energy (Fig. 2). With insignificant surface stress (η = 0 curve), a transition to brittle behavior is almost never observed. This is precisely the case with the bare Al, $CH_3(3)$, and $CH_3(6)$ SAM films.

Second, even moderate surface stress, induced by self-assembly, can result in segmentation (see Fig. 4B). In the present case, this transition occurs at an angle of $\phi = \pi/4$ for η = 1.2. Longer chain length implies larger η (*28*), explaining the observed chain length dependence for the $CH_3(10)$, $CH_3(16)$, and SA(17) SAM films. Furthermore, the transition occurs at a smaller $\eta \sim 0.05$ if the remote stress is assumed tensile (mode I loading), rather than the conservatively assumed remote shear stress loading (τ_S) as in the present case. Preliminary estimates of the surface stress induced by SAM molecules chemisorbing onto an aluminum oxide surface suggest that these values of η are not unreasonable.

These continuum-level predictions of the role of surface stress are reinforced by atomistic simulations of plane-strain loading of a notched Al workpiece with and without adsorbate film (see Fig. 4C). For Al, the embedded atom method interatomic potential was used, with adsorbate atoms forming a Lennard-Jones solid. Surface stress at the notch tip was induced using a lattice mismatch between Al and adsorbate atoms. A small region (two interatomic spacings) at the notch tip was left free of any adsorbate atoms to generate the surface stress heterogeneity at the notch tip.

Figure 4C shows notch behavior without (top row) and with adsorbate (bottom row). When remote load is increased so that the stress intensity factor $K_I = 0.4$ MPa$\sqrt{\text{m}}$, the notch emits an edge dislocation ($\frac{1}{2}$ < 110 >) along the {110} slip plane (frame 2, dislocation core marked yellow), as expected of a ductile metal-like aluminum. The notch is blunted by continuous dislocation emission (top row, frame 3). However, with adsorbate-induced surface stress of $f = +3$ N/m, the notch-tip behavior changes drastically (Fig. 4C, bottom row)—in place of dislocation emission, rapid crack propagation now occurs from the tip (bottom row, frames 2 and 3). This observation is analogous to the surface stress–driven brittle behavior predicted by the continuum model.

DISCUSSION

The results strongly point to the central role of a tensile surface stress in causing the embrittlement. Common mechanisms proposed for MC effects usually involve two components—a mechanical contribution from the external loading and a chemical part that either lowers surface energy or otherwise has a corrosive effect at the notch tip. Our shear deformation experiments with SAMs have unequivocally shown that the "chemistry" of the molecule, controlled by the head/terminal groups, does not influence the workpiece ductility. Rather, the long-chain organic molecules induce a mechanical surface stress on the workpiece that inhibits dislocation

emission, leading to apparent embrittlement of the metal surface. The result is a transition to segmented flow with lowered deformation forces—the MC effect.

That the apparent film-induced embrittlement is driven by mechanical tensile surface stress, as opposed to corrosive action, could well be the case in many stress corrosion phenomena, too (*40*), making this mechanism of quite general applicability. In addition, one can envisage controlling MC effects using external fields, not unlike electrochemically induced deformation effects in nanoporous metals (*41*). Nonetheless, the SAM-metal combination studied in our work is unique for multiple reasons. First, it shows that nanoscale changes in film chemistry can have a profound impact on the macroscale mechanical behavior of relevance to wear and material removal processes. Second, and more practically, it allows independent control of surface energy and surface stress, via the head/terminal group and chain length, respectively. These systems should be of value as general molecular probes for studying adsorption-induced deformation phenomena, in addition to the usual SAM-based surface engineering applications. Designer organic media could be formulated to enhance the capability of deformation, machining, and comminution processes for metals. Preliminary work has already demonstrated the utility of such media in greatly improving the machining of difficult-to-cut metals.

MATERIALS AND METHODS

The experimental framework for applying the simple shear deformation uses 2D (plane strain) peeling/cutting, in which a hard wedge (tool) is moved relative to a workpiece at velocity V_0 to remove a strip of material (chip) (see Fig. 1E). Chip formation occurs by simple shear imposed over a narrow deformation zone, as shown in the figure. The wedge face is fixed normal to V_0, with the face making an angle α with the vertical (rake angle). The workpiece material is constrained on one side by an optically transparent glass block, while being plastically deformed (sheared). The depth of material peeled (undeformed chip thickness, h_0) was set nominally at 50 μm; the exact h_0 was obtained by direct measurement. A nominal sliding velocity V_0 = 5 mm/s was used in all of the experiments; at this small velocity, the deformation is essentially quasi-static and temperature effects are negligible.

The material (plastic flow) in the workpiece was observed in situ at high resolution using an optical microscope coupled to a high-speed complementary metal-oxide semiconductor (CMOS) camera (Photron WX-100). The region of interest, the deformation zone, and adjoining areas were illuminated by a 120-W halogen lamp. A frame rate of 500 frames per second was used, and the spatial resolution was 1.1 μm per pixel. The camera output was high-speed image sequences of the material flow. The high-speed image sequences were analyzed using methods of DIC to obtain accurate interframe material displacements. From the displacement fields, a comprehensive record of material velocity, strain rate, and strain field histories was derived, enabling quantitative characterization of material deformation. The flow was visualized using streaklines, pixel-level strain, and strain-rate fields. A streakline is defined as the locus of a fixed set of material points, as they are convected during material deformation.

The workpiece material was commercially pure aluminum (Al 1100, 99.0% pure, McMaster Carr) in the form of a plate of dimensions 75 mm (length parallel to V_0) by 25 mm by 3 mm (width, into the plane) (see Fig. 1E). It was annealed in a furnace at 550°C for 4 hours and oven cooled to room temperature, before the shearing. The initial hardness of the Al was 23 HV, and the grain size was 200 μm. The hard wedge was made of WC-Co cemented carbide (Tungaloy JVGR200F-TH10) with edge radius <5 μm. Out-of-plane (side) flow of the workpiece was prevented using an optically transparent glass block, which acted as a constraint; this also ensured plane-strain deformation and a clear plane of focus for the imaging. All of the experiments were done at room temperature (T = 300 K) without any lubricant. The cutting force (parallel to V_0) and the thrust force (perpendicular to V_0) were measured using a piezoelectric dynamometer (Kistler 9257B). The cutting force is the power component of the force and provides a direct measure also of the energy dissipated in the shearing energy. The measured forces served to quantify a key attribute of the MC effect, besides providing an assessment of flow modes, flow transitions, and flow stability.

Preparation of SAMs

Before depositing the SAM films, the Al workpiece was ultrasonically cleaned in an ethanol bath for 5 min and in pure water for 5 min. Slightly different procedures were followed to deposit the silane head SAMs and the stearic acid SAMs.

Silane head SAM

The Al workpiece surface was subjected to a plasma irradiation treatment (He gas, 100 Pa, 200 W, 120 s) to increase the density of -OH groups on the surface; this is necessary for the aluminum (oxide) to form a strong bond with the silane-based SAM molecules. Five different chemical agents for silane head SAMs—trichloro(propyl)silane [CH_3(3)], trichloro(hexyl)silane [CH_3(6)], trichloro(octyl)silane [CH_3(8)], trichloro(decyl)silane [CH_3(10)], and trichloro(hexadecyl)silane [CH_3(16)]—procured from Sigma-Aldrich, were used to form SAMs with different lengths of hydrocarbon chain. Next, a 1 mM solution of a particular SAM molecule was prepared in ethanol. In addition to the SAM molecule, dibutylin dilaurate was used as a catalyst and *N*-(1,3-dimethylbutylidene)-3-triethoxysilyl-1-propanamine was used as a promoter, each mixed into the ethanol solution at a concentration of 1 mM each (*31*). The Al workpiece was then immersed in this solution for 1 hour, followed by air-drying at room temperature (T = 300 K) for 12 hours. Last, the workpiece was again cleaned ultrasonically in an ethanol bath for 5 min, and in pure water for 5 min, to complete the sample preparation.

Stearic acid (octadecanoic acid) SAM

A 1 mM solution of stearic acid in ethanol was first prepared without use of any catalyst or promoter. The Al workpiece was then immersed in this solution for 1 hour, followed by air-drying at room temperature (T = 300 K) for 12 hours. Last, the workpiece was again cleaned ultrasonically in an ethanol bath for 5 min, and in pure water for 5 min, to complete the sample preparation.

SUPPLEMENTARY MATERIALS

Supplementary material for this article is available at http://advances.sciencemag.org/cgi/content/full/6/51/eabc8900/DC1

REFERENCES AND NOTES

1. D. Tabor, Babylonian lecanomancy: An ancient text on the spreading of oil on water. *J. Colloid Interface Sci.* **75**, 240–245 (1980).
2. J. E. Greene, Organic thin films: From monolayers on liquids to multilayers on solids. *Phys. Today* **67**, 43–48 (2014).

3. H. Rackham, *Pliny: Natural History* (Harvard Univ. Press, 1938), vol. 1, p. 361.
4. C. Tanford, *Ben Franklin Stilled the Waves* (Oxford Univ. Press, 2004).
5. P. Behroozi, K. Cordray, W. Griffin, F. Behroozi, The calming effect of oil on water. *Am. J. Phys.* **75**, 407–414 (2007).
6. A. R. C. Westwood, Tewksbury lecture: Control and application of environment-sensitive fracture processes. *J. Mater. Sci.* **9**, 1871–1895 (1974).
7. R. M. Latanision, Surface effects in crystal plasticity: General overview, *Surface Effects in Crystal Plasticity*, R. M. Latanision, J. T. Fourie, Eds. (Nordhoff, 1977), pp. 3–48.
8. S. Lynch, Hydrogen embrittlement phenomena and mechanisms. *Corrosion Rev.* **30**, 105–123 (2012).
9. J. Luo, H. Cheng, K. M. Asl, C. J. Kiely, M. P. Harmer, The role of a bilayer interfacial phase on liquid metal embrittlement. *Science* **333**, 1730–1733 (2011).
10. W. Rostoker, J. McCaughey, H. Markus, *Embrittlement by Liquid Metals* (Reinhold Pub. Corp., 1960).
11. D. H. Bangham, The Gibbs adsorption equation and adsorption on solids. *Trans. Faraday Soc.* **33**, 805–811 (1937).
12. G. Y. Gor, N. Bernstein, Revisiting Bangham's law of adsorption-induced deformation: Changes of surface energy and surface stress. *Phys. Chem. Chem. Phys.* **18**, 9788–9798 (2016).
13. R. Roscoe, Strength of metal single crystals. *Nature* **133**, 912 (1934).
14. P. Rehbinder, New physico-chemical phenomena in the deformation and mechanical treatment of solids. *Nature* **159**, 866–867 (1947).
15. R. M. Latanision, R. H. Jones, *Chemistry and Physics of Fracture* (Springer, 1987).
16. A. R. C. Westwood, J. J. Mills, Survey lecture: Applications of chemomechanical effects to fracture-dependent industrial processes, *Surface Effects in Crystal Plasticity*, R. M. Latanision, J. T. Fourie, Eds. (Nordhoff, 1977).
17. R. A. Oriani, On the possible role of the surface stress in environmentally induced embrittlement and pitting. *Scr. Metall.* **18**, 265–268 (1984).
18. P. A. Rehbinder, E. D. Shchukin, Surface phenomena in solids during deformation and fracture processes. *Prog. Surf. Sci.* **3**, 97–104 (1972).
19. J. R. Rice, J.-S. Wang, Embrittlement of interfaces by solute segregation. *Mater. Sci. Eng. A* **107**, 23–40 (1989).
20. H.-P. Chen, R. K. Kalia, E. Kaxiras, G. Lu, A. Nakano, K.-i. Nomura, A. C. T. van Duin, P. Vashishta, Z. Yuan, Embrittlement of metal by solute segregation-induced amorphization. *Phys. Rev. Lett.* **104**, 155502 (2010).
21. F. Rosei, M. Schunack, Y. Naitoh, P. Jiang, A. Gourdon, E. Laegsgaard, I. Stensgaard, C. Joachim, F. Besenbacher, Properties of large organic molecules on metal surfaces. *Prog. Surf. Sci.* **71**, 95–146 (2003).
22. H. Yeung, K. Viswanathan, W. D. Compton, S. Chandrasekar, Sinuous flow in metals. *Proc. Natl. Acad. Sci. U.S.A.* **112**, 9828–9832 (2015).
23. A. Udupa, K. Viswanathan, M. Saei, J. B. Mann, S. Chandrasekar, Material-independent mechanochemical effect in the deformation of highly strain-hardening metals. *Phys. Rev. App.* **10**, 014009 (2018).
24. A. Udupa, K. Viswanathan, J. M. Davis, M. Saei, J. B. Mann, S. Chandrasekar, A mechanochemical route to cutting highly strain-hardening metals. *Tribol. Lett.* **67**, 4 (2019).
25. N. Beckmann, P. A. Romero, D. Linsler, M. Dienwiebel, U. Stolz, M. Moseler, P. Gumbsch, Origins of folding instabilities on polycrystalline metal surfaces. *Phys. Rev. Appl.* **2**, 064004 (2014).
26. A. Ulman, Formation and structure of self-assembled monolayers. *Chem. Rev.* **96**, 1533–1554 (1996).
27. R. Berger, E. Delamarche, H. P. Lang, C. Gerber, J. K. Gimzewski, E. Meyer, H.-J. Güntherodt, Surface stress in the self-assembly of alkanethiols on gold. *Science* **276**, 2021–2024 (1997).
28. G. Wu, H. Ji, K. Hansen, T. Thundat, R. Datar, R. Cote, M. F. Hagan, A. K. Chakraborty, A. Majumdar, Origin of nanomechanical cantilever motion generated from biomolecular interactions. *Proc. Natl. Acad. Sci. U.S.A.* **98**, 1560–1564 (2001).
29. A. W. Adamson, *Physical Chemistry of Surfaces* (John Wiley & Sons, 1990).
30. D. L. Allara, R. G. Nuzzo, Spontaneously organized molecular assemblies. 1. Formation, dynamics, and physical properties of n-alkanoic acids adsorbed from solution on an oxidized aluminum surface. *Langmuir* **1**, 45–52 (1985).
31. Y.-J. Kim, K.-H. Lee, H. Sano, J. Han, T. Ichii, K. Murase, H. Sugimura, Surface chemical conversion of organosilane self-assembled monolayers with active oxygen species generated by vacuum ultraviolet irradiation of atmospheric oxygen molecules. *Jpn. J. Appl. Phys.* **47**, 307–312 (2008).
32. A. Ulman, *An Introduction to Ultrathin Organic Films: From Langmuir-Blodgett to Self-Assembly* (Academic Press, 2013).
33. C. D. Bain, E. B. Troughton, Y. T. Tao, J. Evall, G. M. Whitesides, R. G. Nuzzo, Formation of monolayer films by the spontaneous assembly of organic thiols from solution onto gold. *J. Am. Chem. Soc.* **111**, 321–335 (1989).
34. D. K. Owens, R. C. Wendt, Estimation of the surface free energy of polymers. *J. Appl. Polym. Sci.* **13**, 1741–1747 (1969).
35. The specific cutting force for hard steel is ~4050 MPa, translating to a force of 364 N for h_0 of 50 μm and width of 3 mm used in our experiments. See link for more information: http://www.mitsubishicarbide.net/contents/mhg/enuk/html/product/technical.
36. M. C. Shaw, *Metal Cutting Principles* (MIT Press, 1957).
37. J. Fritz, Cantilever biosensors. *Analyst* **133**, 855–863 (2008).
38. J. R. Rice, R. Thomson, Ductile versus brittle behaviour of crystals. *Philos. Mag.* **29**, 73–97 (1974).
39. F. Spaepen, Interfaces and stresses in thin films. *Acta Mater.* **48**, 31–42 (2000).
40. N. Badwe, X. Chen, D. K. Schreiber, M. J. Olszta, N. R. Overman, E. K. Karasz, A. Y. Tse, S. M. Bruemmer, K. Sieradzki, Decoupling the role of stress and corrosion in the intergranular cracking of noble-metal alloys. *Nat. Mater.* **17**, 887–893 (2018).
41. H.-J. Jin, J. Weissmüller, A material with electrically tunable strength and flow stress. *Science* **332**, 1179–1182 (2011).
42. R. Thomson, T.-J. Chuang, I.-H. Lin, The role of surface stress in fracture. *Acta Metall.* **34**, 1133–1143 (1986).
43. S. Plimpton, Fast parallel algorithms for short-range molecular dynamics. *J. Comput. Phys.* **117**, 1–19 (1995).

Acknowledgments: We acknowledge R. Latanision (MIT/Exponent) and K. Kendall, FRS (University of Birmingham/Adelan, UK) for discussions and constructive comments on the manuscript. We thank Y. Ohkubo (Osaka University, Japan) for assistance with preparation of the SAM films, and M. Ansari [Indian Inst. Sci. (IISc), India] for help with model calculations. **Funding:** The work at Purdue was supported, in part, by U.S. Department of Energy EERE program award DE-EE000786 and at IISc by SERB grant CRG/2018/002058, Government of India. J.M.D. acknowledges support from the DoD, Naval Surface Warfare Center, Crane Division, under the NISE Program and the DoD SMART Scholarship-for-Service Program. **Author contributions:** T.S. and A.U. designed and carried out the experiments with the molecular films. A.U. and K.V. formulated the model for the ductile-to-brittle transition and conducted analysis with the model. S.C. supervised the work. All of the authors were involved in analysis of the data, formulation of hypothesis and conclusions, and writing of the manuscript. **Competing interests:** The authors declare that they have no competing interests. **Data and materials availability:** All data needed to evaluate the conclusions in the paper are present in the paper and/or the Supplementary Materials. Additional data related to this paper may be requested from the authors.

Submitted 21 May 2020
Accepted 2 November 2020
Published 16 December 2020
10.1126/sciadv.abc8900

Citation: T. Sugihara, A. Udupa, K. Viswanathan, J. M. Davis, S. Chandrasekar, Organic monolayers disrupt plastic flow in metals. *Sci. Adv.* **6**, eabc8900 (2020).

Science Advances

Organic monolayers disrupt plastic flow in metals

Tatsuya Sugihara, Anirudh Udupa, Koushik Viswanathan, Jason M. Davis and Srinivasan Chandrasekar

Sci Adv **6** (51), eabc8900.
DOI: 10.1126/sciadv.abc8900